

See discussions, stats, and author profiles for this publication at: <https://www.researchgate.net/publication/262226750>

# Replica-Exchange Molecular Dynamics Simulation of Basic Fibroblast Growth Factor Adsorption on Hydroxyapatite

ARTICLE *in* THE JOURNAL OF PHYSICAL CHEMISTRY B · JUNE 2014

Impact Factor: 3.3 · DOI: 10.1021/jp501463r · Source: PubMed

---

CITATIONS

5

---

READS

30

2 AUTHORS, INCLUDING:



Jian Zhou

South China University of Technology

84 PUBLICATIONS 1,593 CITATIONS

SEE PROFILE

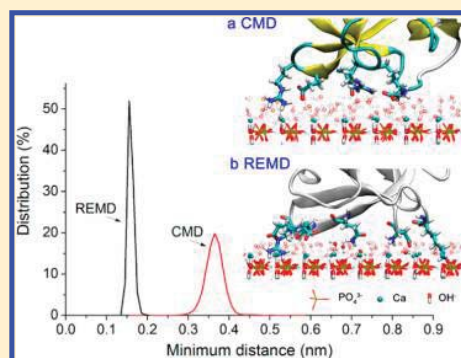
## Replica-Exchange Molecular Dynamics Simulation of Basic Fibroblast Growth Factor Adsorption on Hydroxyapatite

Chenyi Liao and Jian Zhou\*

School of Chemistry and Chemical Engineering, Guangdong Provincial Key Lab for Green Chemical Product Technology, South China University of Technology, Guangzhou, 510640, P. R. China

## S Supporting Information

**ABSTRACT:** The adsorption of basic fibroblast growth factor (bFGF) on the hydroxyapatite (001) surface was investigated by a combination of replica-exchange molecular dynamics (REMD) and conventional molecular dynamics (CMD) methods. In CMD, the protein cannot readily cross the surface water layer, whereas in REMD, the protein can cross the adsorption barrier from the surface water layer and go through weak, medium, then strong adsorption states with three energetically preferred configurations: heparin-binding-up (HP-up), heparin-binding-middle (HP-middle), and heparin-binding-down (HP-down). The HP-middle orientation, with the strongest adsorption energy ( $-1149 \pm 40$  kJ·mol<sup>-1</sup>), has the largest adsorption population (52.1–52.6%) and exhibits the largest conformational charge (RMSD of  $0.26 \pm 0.01$  nm) among the three orientations. The HP-down and HP-up orientations, with smaller adsorption energies of  $-1022 \pm 55$  and  $-894 \pm 70$  kJ·mol<sup>-1</sup>, respectively, have smaller adsorption populations of 27.4–27.7% and 19.7–20.5% and present smaller RMSD values of  $0.21 \pm 0.01$  and  $0.19 \pm 0.01$  nm, respectively. The convergent distribution indicates that nearly half of the population (in the HP-middle orientation) will support both FGF/FGFR and DGR–integrin signaling and another half (in the HP-up and HP-down orientations) will support DGR–integrin signaling. The major population (~80%) has the protein dipole directed outward. In the strong adsorption state, there are usually 2 to 3 basic residues that form the anchoring interactions of  $210\text{--}332$  kJ·mol<sup>-1</sup> per residue or that are accompanied by an acidic residue with an adsorption energy of  $\sim 207$  kJ·mol<sup>-1</sup>. Together, the major bound residues form a triangle or a quadrilateral on the surface and stabilize the adsorption geometrically, which indicates topologic matching between the protein and HAP surfaces.



## 1. INTRODUCTION

One goal in orthopedic surgery is to develop implants that can enhance bone regeneration and heal massive bone defects caused by arthritis, tumors, and trauma. Hydroxyapatite ( $\text{Ca}_{10}(\text{PO}_4)_6(\text{OH})_2$ , HAP), as the primary mineral component of human bones and teeth enamel, is one of the most widely used bioactive ceramics for bone substitutes.<sup>1,2</sup> It is essential for bone substitutes to mimic the bone that possesses the unique capacity to regenerate from bone stem cells and growth factors. Cell growth factors are considered to be the most attractive type of bioactive agents for the regulation of angiogenesis and osteogenesis. Loading growth factors on HAP scaffolds allows for the development of tissue-engineering scaffolds that stimulate osteoprogenitor cells to differentiate into osteoblasts, which then begin new bone formation.<sup>3</sup>

Basic fibroblast growth factor (bFGF or FGF2) is a member of fibroblast growth factor (FGF) family. It is a powerful modulator of cell growth and the formation of new blood vessels (angiogenesis), which speed up the wound healing process. FGFs exert multiple biological functions, including cellular proliferation, survival, migration, and differentiation, through FGF/FGF-receptor signaling pathway.<sup>4</sup> Binding domains and sites for bFGF receptor and heparan sulfate

proteoglycans (HSPG) or heparin have been identified.<sup>5</sup> The heparin-binding site is also called the low-affinity binding site.<sup>6</sup> When FGF binds to HSPG on a cell's surface, it protects FGF from denaturation caused by heat or proteolytic enzyme interactions. Furthermore, when heparin binds to a FGF receptor (FGFR), it enhances the binding affinity of FGF to FGFR and is coupled to the FGF–FGFR interaction.<sup>7</sup> Subsequent binding of a second FGF molecule may then lead to a more stable 2:2 FGF–FGFR dimer complex.<sup>8</sup> In addition, bFGF is intricately involved in cell adhesion and growth. bFGF contains two Asp–Gly–Arg (DGR) sequences that represent the inverse triplet of RGD (the cell recognition site of fibronectin). DGR-containing peptides have been found to compete with adhesive proteins for integrin recognition.<sup>9,10</sup>

Recently, bFGF has attracted considerable interest in tissue regeneration involving in angiogenesis, bone formation, and bone ingrowth.<sup>11–14</sup> It has been shown that bFGF-coated HAP materials allow osteoblastic cells to adhere and proliferate well, to upregulate significantly the expression of genes associated

Received: February 11, 2014

Revised: April 25, 2014

Published: May 12, 2014

with early stage bone formation, and to reach a level comparable to that found in autogenous bone during bone ingrowth.<sup>11–16</sup> Although bFGF plays an important role in the regulation of bone metabolism, its adsorption mechanism on HAP at the atomic level has so far received very little attention. Detailed information on the adsorption orientation, conformation, and interaction of bFGF with the HAP surface is not yet clear, although these characteristics greatly impact the biological activity of bFGF in FGF/FGFR signaling and cell adhesion.

The (001) face is one of the major surfaces of HAP materials<sup>17,18</sup> and is much more stable than the (100) face.<sup>19,20</sup> A related study has shown that the hierarchical micro-nanohybrid surfaces of HAP, in which the (001) face is the dominant plane, significantly promoted protein adsorption and cell proliferation in comparison to that from the traditional flat and dense sample.<sup>18</sup> The microstructure of the HAP surface could be more complicated than that of a plain surface, and surfaces in the same direction have been tailored into different textures.<sup>21–23</sup> The effect of surface defects on protein adsorption behavior could be particularly important because the surface topology may affect the biological activity of adsorbed proteins.<sup>24,25</sup>

Protein–surface interactions are a fundamental issue in various fields and devices. The orientation of an adsorbed protein on a medical device, for example, greatly determines the activity of the protein.<sup>26–31</sup> Molecular simulation is well-suited to provide insight about protein behavior on a surface. Simulating a protein–surface system is usually computationally expensive because of the complexity of proteins and the huge number of water molecules, which makes the adsorption energy landscape rugged. Conventional Monte Carlo (MC) and molecular dynamics (MD) simulations in a canonical ensemble may become trapped in a local energy minima, where there is a large energy barrier between the stable state and any other possible metastable state. As a result, they may fail to sample a representative set of the global free energy minima of phase space.<sup>32,33</sup> Replica-exchange (also parallel tempering) techniques are being increasingly used to improve the sampling for simulations of peptides and small proteins.<sup>32–35</sup> Although some studies have shown that issues like convergence,<sup>34</sup> heterogeneity,<sup>34</sup> and sampling efficiency exist for these techniques,<sup>35</sup> they facilitate the exploration of configuration space through higher temperatures and allow the system to cross barriers not readily crossed at the target temperature on a given time scale. Thus, this approach was applied here to a protein–surface system to overcome the adsorption barrier and to achieve the preferred adsorption states.

In this work, bFGF adsorption on the HAP surface was carried out by a combination of replica-exchange molecular dynamics (REMD) and conventional MD (CMD) methods. A first-stage REMD method was applied to overcome the adsorption barrier and to search for a representative set of preferred adsorption states. The preferred adsorption states were further investigated in second-stage REMD and CMD simulations using the adsorption energy, orientation and conformation, and FGFR–integrin binding accessibility of bFGF in a specific orientation as well as the adsorbed residues, including possible topological matching with the surface. This work could provide some understanding of the adsorption mechanism of bFGF on apatite surfaces at the molecular level.

## 2. METHODS

**2.1. Theory.** The general idea of REMD is to simultaneously simulate  $M$  replicas of a system at successive temperatures and to randomly exchange the complete configuration of two adjacent replicas at regular intervals with the probability<sup>32</sup>

$$P(U_i, T_i \leftrightarrow U_{i+1}, T_{i+1}) = \min(1, \exp(\Delta\beta\Delta U)) \quad (1)$$

where  $\Delta\beta = (1/k_B)((1/T_{i+1}) - (1/T_i))$  is the difference between the inverse temperatures of neighboring replicas;  $\Delta U = U_{i+1} - U_i$  corresponds to the potential energy difference of neighboring replicas. Each replica typically runs MD in the canonical ensemble at a different temperature,  $T_i$ . In general,  $T_1 < T_2 < \dots < T_M$ . After an exchange, the new momentum,  $p_{i,\text{new}}$ , for replica  $i$  is scaled by

$$p_{i,\text{new}} = (T_{\text{new}}/T_{\text{old}})^{0.5} p_{i,\text{old}} \quad (2)$$

where  $p_{i,\text{old}}$  is the old momentum for replica  $i$ ;  $T_{\text{old}}$  and  $T_{\text{new}}$  are the temperatures of the replicas before and after the swap, respectively. This procedure ensures that the average kinetic energy remains equal to  $3Nk_B T/2$ .

**2.2. Surface Model.** The original crystal structure of HAP ( $P6_3/m$ ) was extracted from the American Mineralogist Crystal Structure Database<sup>36</sup> with unit cell parameters of  $a = b = 0.943$  nm and  $c = 0.688$  nm. In the HAP crystal, a Ca ion that has three oxygen atoms as its first neighbors is labeled as Ca(1); other Ca ions are labeled as Ca(2).<sup>21</sup> The defective HAP (001) surface with Ca(1) vacancies is cut with half of the Ca(1) ions presented in the upper and lower interfaces<sup>21</sup> (see Figure S1 in the Supporting Information) using Materials Studio 4.4 (Accelrys, Inc.). The net charge of the HAP slab is zero. The HAP surface is hydrophilic.<sup>21</sup> Charge density maps of the defective HAP (001) surface with an outward H or O atom in the OH column were calculated and are shown in Figure S2 in the Supporting Information. The Ca(1) vacancy on the HAP surface is surrounded by a triad of phosphate ions (see Figure S2 in the Supporting Information).

All-atom force field parameters for HAP were derived from Hauptmann's model,<sup>37</sup> which was fitted into the Lennard–Jones potential<sup>38</sup> and used here. The HAP force field parameters and the evaluation are appended in the Supporting Information (S1).

**2.3. Simulation Details.** The crystal structure of bFGF was taken from the Protein Data Bank (PDB code: 2BFH).<sup>39</sup> The structure of bFGF is composed of 12 anti-parallel  $\beta$ -strands strongly bound by small loops. It consists of 127 amino acid residues from residue 19 to 146. It carries 11 positive charges (+11e) under neutral conditions. The possible heparin-binding site comprises five basic residues: Lys119, Arg120, Lys125, Lys129, and Lys135.<sup>39</sup>

All simulations were performed with GROMACS 4.5.3 software<sup>40</sup> using the OPLS force field<sup>41</sup> supplemented with the HAP parameters.<sup>21,23</sup> The HAP slab contains  $7 \times 7 \times 3$  units ( $6.6 \times 6.53 \times 2.06$  nm<sup>3</sup>). bFGF was initially put 5 Å above the HAP surface. A periodic box of  $6.6 \times 6.53 \times 9.0$  nm<sup>3</sup> was solvated with explicit water in the SPC/E model.<sup>42</sup> The SPC/E water model in combination with OPLS-AA performed fairly well in protein structure and water diffusivity.<sup>43</sup> This indicates that the results from our systems should not vary much using the SPC/E water model. Eleven Cl<sup>−</sup> ions were added as counterions to neutralize the system. The whole system contains 36 209 atoms and 8911 water molecules. The cutoff

distance for the short-range neighbor list is 1.1 nm. The VDW cutoff distance is 1.1 nm. The long-range electrostatic interactions were calculated by the particle-mesh Ewald method,<sup>44</sup> with a grid spacing of  $\sim 0.12$  nm and a real-space cutoff of 1.1 nm. Long-range dispersion corrections for energy and pressure were applied. Bonds in protein and surface were constrained using the LINCS algorithm.<sup>45</sup> The simulations were carried out with a time step of 1 fs in the NVT ensemble. The Nose–Hoover thermostat<sup>46,47</sup> was used for temperature coupling. The simulations comprise three parts:

- (1) First-stage REMD simulations were performed to gain energetically favorable samples. Forty eight replicas were used with temperatures ranging from 310 to 405 K at intervals of 1.8–2.2 K. The temperature distribution was determined using the algorithm proposed by Patriksson and van der Spoel,<sup>48</sup> given the lowest (310 K) and highest (405 K) temperatures, the system size, and an acceptance ratio ( $\sim 20\%$ ). The target the temperature was 310 K. Before exchange, a complete workflow (i.e., energy minimization (steepest descent algorithm), 200 ps NVT pre-equilibration with the protein position restrained, and 500 ps CMD) was conducted for each replica. Then, REMD (48 replicas  $\times$  80 ns per replica) simulations were performed, with coordinates and energies recorded every 10 ps. Replicas of neighboring temperatures attempt exchange every 1000 steps (1 ps) with an acceptance ratio of around 17–23%.
- (2) Second-stage REMD simulations were performed using the three typical energetically favorable configurations achieved in the first-stage REMD. The energetically favorable samples were used as the replicas, with the same temperature interval (1.8–2.2 K) and simulation setup in the 3 replicas  $\times$  20 ns per replica REMD.
- (3) Adsorbed or unadsorbed properties were investigated by CMD simulations: 100 ns CMD was performed on each energetically favorable sample from REMD, 200 ns CMD of the same initial configuration from the first-stage REMD was carried out at 310 K as a comparison group, and 100 ns CMD simulation of bFGF in bulk water at 310 K was also performed.

### 3. RESULTS AND DISCUSSION

The adsorption tendencies of bFGF on the HAP surface in the first-stage REMD simulations are presented using the minimum protein–HAP distances and adsorption energies in Figure 1 and using protein orientations in Figure 2. The minimum protein–HAP distance reflects the protein–surface closeness and adsorption strength. The adsorption strength is characterized by the adsorption energy. The orientation of an adsorbed protein on a surface is quantitatively characterized by the orientation angle ( $\theta$ ), which is defined as the angle between the normal unit vector to the surface and the unit vector along the dipole of a protein.<sup>27,30,49</sup>  $\cos \theta$  is calculated for each possible orientation. The minimum protein–HAP distance distributions by CMD and REMD are compared in Figure 3. Structural changes in energetically favorable states are displayed in Figure 4. Backbone root-mean-square deviation (RMSD) was used to characterize the conformational change in bFGF with respect to the crystal structure. The accessibility of the heparin-binding site and two DGR sequences in preferred orientations is exhibited in Figure 5. Configurations of the bFGF–FGFR–heparin ternary complex in its preferred

orientations are shown in Figure 6. Major adsorbed residues and topological matching in the preferred orientations are illustrated in Figure 7. The orientations, adsorption energy (protein–HAP interactions), and RMSD in the preferred orientations are presented in Table 1. Major adsorption residues with their relative residence times, residue–HAP interactions, hydrogen bonds, residue–HAP distances, and adsorption sites are included in Table 2.

**3.1. Adsorption Tendencies in REMD.** The energy overlap and replica exchange at temperatures ranging from 310 to 405 K are appended in Figures S3 and S4 in the Supporting Information. The temperature distribution interval allows for sufficient configurational exchange between replicas. When a protein adsorbs on the HAP surface, it may adsorb 0.35–0.37 nm above the surface under weak adsorption or 0.15–0.17 nm from the surface under some stronger interactions.<sup>50</sup> The protein–HAP distance evolution in Figure 1a indicates that after swapping between replicas for about 40

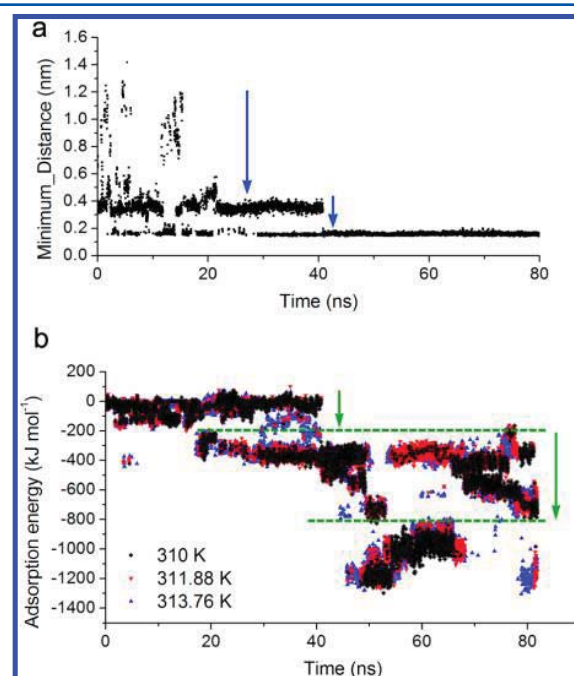


**Figure 1.** Time evolution of the (a) minimum protein–HAP distance at 310 K; (b) adsorption energies at 310, 311.88, and 313.76 K by first-stage REMD.

ns it converges to bound states with an average distance of around 0.15–0.17 nm. As indicated in Table 2, with residue–HAP distances of around 0.15–0.17 nm, bFGF is likely to form hydrogen bonds with the HAP surface through interactions between the basic residues (arginine or lysine) and the phosphate ions, especially the triads of phosphate ions around the Ca vacancies on the HAP surface (see Figure S2 in the Supporting Information).<sup>50</sup>

As indicated in Figure 1b, the adsorption energy evolution of three adjacent replicas, 310, 311.88, and 313.76 K, presents similar hierarchical energies. Accordingly, the adsorptions are divided into three states: weak (approximately  $-200$  kJ·mol<sup>-1</sup>), medium ( $-200$  to  $-800$  kJ·mol<sup>-1</sup>), and strong ( $-800$  to  $-1400$  kJ·mol<sup>-1</sup>) adsorption states. For the weak adsorption state, bFGF mainly adsorbs 0.35–0.37 nm above the HAP surface (see Figure S5 in the Supporting Information), with absolute



adsorption energy values of less than 200 kJ·mol<sup>-1</sup> (Figure 1a,b). For the medium adsorption state, there are 1 to 2 basic residues that form hydrogen bonds with the triads of the phosphate ions in the Ca vacancies (see Figure S6 in the Supporting Information), which we call anchoring interactions<sup>50</sup> because the way that the basic residue sticks into the Ca(1) vacancy is like an anchor (Figure 7). For the strong adsorption state, there are usually 2 to 3 basic residues that form the anchoring interactions or that are accompanied by binding of an acidic residue (Figures 5 and 7). When a basic residue forms the anchoring interactions, it contributes 210–350 kJ·mol<sup>-1</sup> to the adsorption (Table 2). Also, the strong binding between an acidic residue and a Ca ion would contribute ~209 kJ·mol<sup>-1</sup> to the adsorption (Table 2). Thus, the absolute adsorption energy in the strong adsorption state is usually larger than 800 kJ·mol<sup>-1</sup>. The medium adsorption state exhibits changeable orientations with two bound residues (see Figure S6 in the Supporting Information), whereas the orientations are stabilized in the strong binding state by three or more bound residues that together impart geometrical stability (Figures 5 and 7). The swapping initially occurs between the weak and medium adsorption states, and it then further progresses between the medium and strong adsorption states (Figure 1b). We propose that the metastable medium adsorption state will finally progress to the strong adsorption state with the stabilized configurations.

The orientations are investigated in Figure 2. For the initial 20 ns, the orientation space is quasi-ergodically sampled from -1 to 1 by REMD (Figure 2a). The configurations with  $\cos \theta$  around -0.92 to -1.0 are sampled with few populations because the orientations would present large positive adsorption energies and because it is not favorable to find them near the surface (see Figures S7 and S8 in the Supporting Information). After swapping between replicas for about 25 ns,  $\cos \theta$  exhibits a major population at 0–1.0 and a minor population around -0.68 within the 80 ns exchanging time. The adsorption energy contour in Figure 2b shows that there are three preferred orientations, with  $\cos \theta$  at  $0.70 \pm 0.10$ ,  $0.20 \pm 0.20$ , and  $-0.68 \pm 0.10$ , that exhibit strong binding affinities with the surface ( $< -800$  kJ·mol<sup>-1</sup>). The  $\cos \theta$  distributions of the adsorption states at 310, 311.88, and 313.76 K in Figure 2c represent the three preferred orientations. They are labeled as heparin-binding-up (HP-up), heparin-binding-middle (HP-middle), and heparin-binding-down (HP-down), respectively, according to the heparin-binding site position (Figure 2d–f).

To look into the convergent distribution between energetically favorable adsorption samples, typical configurations of the three energetically preferred orientations (Figure 5) were further investigated by second-stage REMD. Second-stage REMD was carried out with the HP-up, HP-middle, and HP-down configurations (Figure 5), swapping at 310, 311.88, and 313.76 K. The convergent orientations, energies, and repeatability for second-stage REMD are appended in the Supporting Information (S3). The convergent orientation distribution indicates that the HP-middle configuration with the strongest adsorption energies ( $-1149 \pm 40$  kJ·mol<sup>-1</sup>; Table 1) has a population of 52.1–52.6%, whereas the HP-down and HP-up configurations with smaller adsorption energies ( $-1022 \pm 55$  and  $-894 \pm 70$  kJ·mol<sup>-1</sup>; Table 1) have populations of 27.4–27.7% and 19.7–20.5%, respectively (Figure 2c). Stronger adsorption energies occupy a larger population in the adsorption.

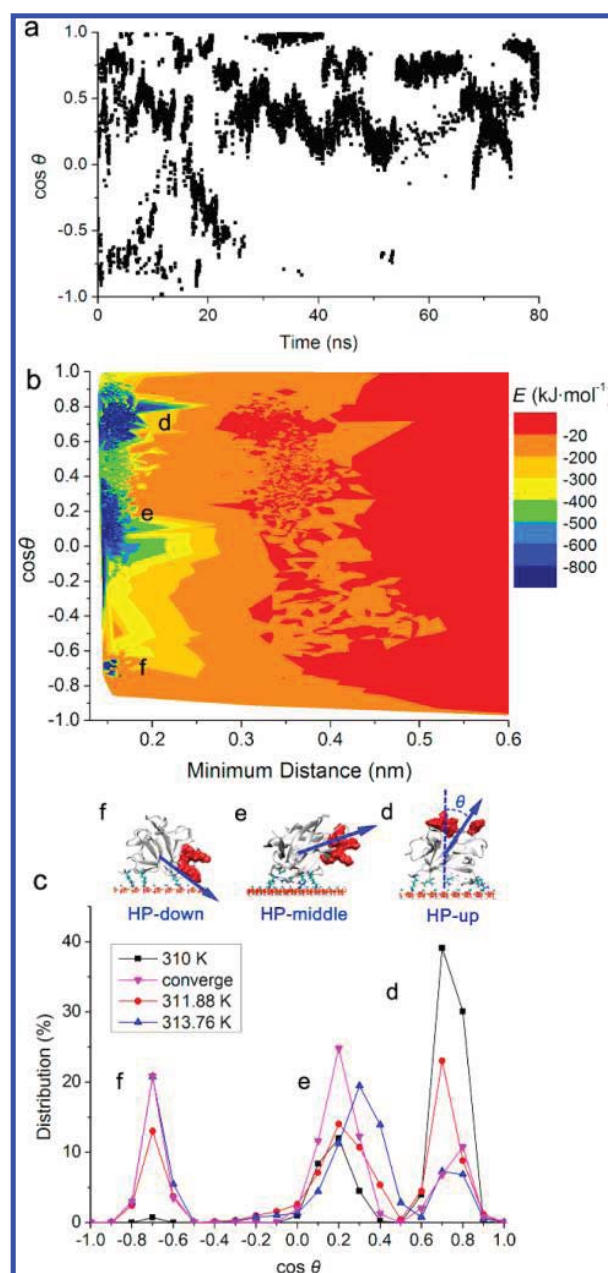


**Figure 2.** (a) Time evolution of the orientation ( $\cos \theta$ ) at 310 K by first-stage REMD; (b) adsorption energy ( $E$ ) contour with related variables (adsorption orientation ( $\cos \theta$ ) and minimum distance ( $< 0.6$  nm)) by first-stage REMD; (c)  $\cos \theta$  distributions of strong binding states at 310, 311.88, and 313.76 K by first-stage REMD and convergent distribution by second-stage REMD. The three preferred orientations are labeled as (d) heparin-binding-up (HP-up), (e) heparin-binding-middle (HP-middle), and (f) heparin-binding-down (HP-down), with  $\cos \theta$  at  $0.70 \pm 0.10$ ,  $0.20 \pm 0.20$ , and  $-0.70 \pm 0.10$ , respectively. The dipole vector is labeled as an arrow from the center of mass of the protein to the dipole direction. A possible heparin-binding site is in red.

The minimum protein–HAP distances achieved in the 200 ns CMD and in first-stage REMD are compared in Figure 3, with illustrations on the right and enlarged views appended in Figure S9 in the Supporting Information. The adsorption energy distributions by CMD and REMD are appended in

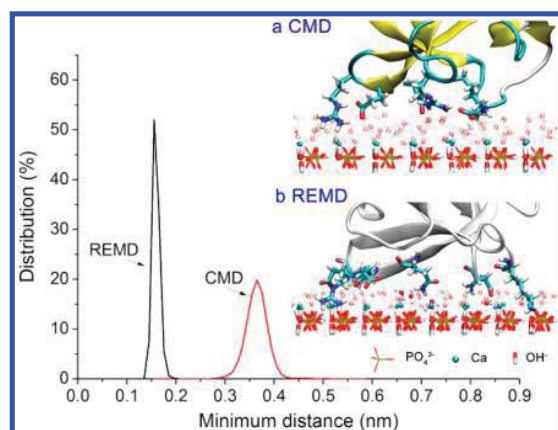


**Figure 3.** Minimum protein–HAP distance distributions by the 200 ns CMD and first-stage REMD (last 40 ns) at 310 K. Illustrations of the protein–HAP distance with water molecules are on the right. The major adsorption residues in CMD are Glu58, Glu59, Arg60, Asp90, Arg109, and Lys110. The upper Ca ions of the HAP slab are shown as blue dots.

Figure S10 in the Supporting Information. Unlike the highly ordered water layer on a  $\text{TiO}_2$  surface,<sup>26,51,52</sup> the water molecules adsorb more freely on the HAP surface. In 200 ns CMD, bFGF adsorbs around 0.35–0.37 nm above the HAP surface under weak protein–HAP interactions (approximately  $-55 \text{ kJ}\cdot\text{mol}^{-1}$ ) and the orientation converges fast at 0.8–1.0 (see Figures S10–S12 in the Supporting Information). By REMD, a significantly closer protein–HAP distance, around 0.15–0.17 nm, was achieved. The major barrier to adsorption may come from the surface water layer. The binding of soluble bFGF<sup>4</sup> to the hydrophilic HAP surface<sup>21</sup> involves the displacement of water molecules between the protein and surface. Under weak adsorption in CMD, bFGF adsorbs above the water layer (Figure 3a). It may take a much longer time scale to reach a more stable adsorption state.<sup>53</sup> However, in REMD, the residue breaks through the water layer and reaches the Ca(1) vacancies (Figure 3b).

In simulations of protein adsorption, the REMD method helps to overcome the adsorption barrier from the water layer, which is not readily crossed by the CMD method in 200 ns. REMD accelerates the sampling for energetically favorable adsorptions, whereas CMD gets trapped in a local energy minimum. Thus, it is quite necessary to perform replica exchange to search for the global adsorption states before CMD is carried out.<sup>49,50</sup>

**3.2. Energetically Favorable Adsorptions.** Three typical energetically favorable configurations in the HP-up, HP-middle, and HP-down orientations were investigated using the orientation, adsorption energy, and backbone RMSD of bFGF in 100 ns CMD. Within the simulation time, the strong binding configurations from REMD remain stable with the orientation, adsorption energy, and protein structure. Superpositions of bFGF (red) on the crystal structure (white) in the HP-up, HP-middle, and HP-down orientations and in bulk water are shown in Figure 4a–d, respectively. The backbone RMSD of bFGF in bulk water is around  $0.11 \pm 0.01 \text{ nm}$ .<sup>54</sup> As shown in Table 1, the HP-middle orientation with the strongest adsorption energy ( $-1149 \pm 40 \text{ kJ}\cdot\text{mol}^{-1}$ ) exhibits the largest conformational change (RMSD of  $0.26 \pm 0.01 \text{ nm}$ ), whereas the HP-down and HP-up orientations that exhibit weaker adsorption energies of  $-1022 \pm 55$  and  $-894 \pm 70 \text{ kJ}\cdot\text{mol}^{-1}$

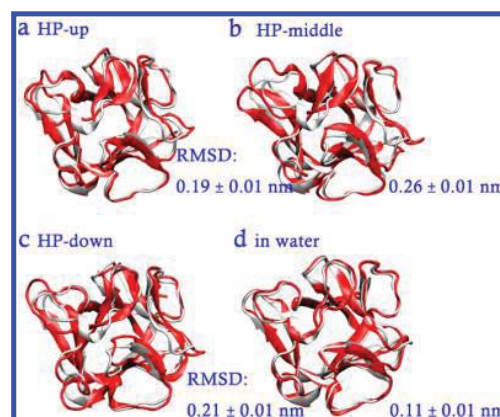


**Figure 4.** Superpositions of bFGF (red) on the crystal structure (white) in the (a) heparin-binding-up (HP-up), (b) heparin-binding-middle (HP-middle), and (c) heparin-binding-down (HP-down) orientations and (d) in water.

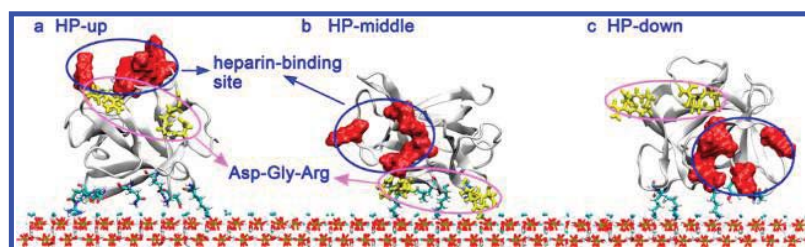
**Table 1.** Orientation, Adsorption Energy ( $E_{\text{HAP-protein}}$ ), and Protein Backbone RMSD in the HP-Up, HP-Middle, and HP-Down Orientations and in Bulk Water

state	orientation ( $\cos \theta$ )	$E_{\text{HAP-protein}}$ ( $\text{kJ}\cdot\text{mol}^{-1}$ )	backbone RMSD (nm)
HP-up	$0.74 \pm 0.06$	$-894 \pm 70$	$0.19 \pm 0.01$
HP-middle	$0.17 \pm 0.09$	$-1149 \pm 40$	$0.26 \pm 0.01$
HP-down	$-0.68 \pm 0.07$	$-1022 \pm 55$	$0.21 \pm 0.01$
in bulk water			$0.11 \pm 0.01$

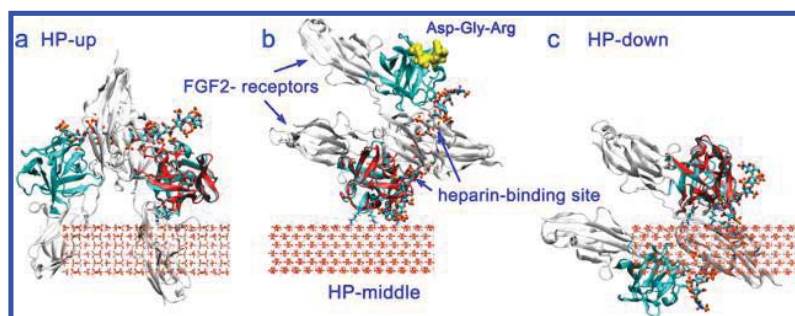
present smaller RMSD values of  $0.21 \pm 0.01 \text{ nm}$  and  $0.19 \pm 0.01 \text{ nm}$ , respectively. Stronger protein–HAP interactions tend to induce a larger conformational change.

Figure 5a–c further presents the accessibility of heparin-binding site and two DGR sequences in the HP-up, HP-middle, and HP-down orientations. As mentioned in the Introduction, DGR mimics the integrin-binding site of fibronectin.<sup>5</sup> To stimulate the integrin signaling pathway for cell adhesion, it has been suggested that the DGR sequence should be exposed to solution.<sup>9,10</sup> As shown in Figure 5, the DGR is accessible in solution in both the HP-up and HP-down orientations, which is beneficial for stimulating cell attachment through integrin binding.<sup>9</sup> DGR is close to the surface in the HP-middle orientation, which is unfavorable for integrin binding.

Both the heparin-binding site and DGR sequences are accessible in the HP-up orientation. Does this mean that this orientation is the most favorable for bFGF bioactivity? We superimposed either of the bFGF molecules in the bFGF–FGFR–heparin complex (PDB code: 1FQ9)<sup>55</sup> on the adsorbed bFGF structure on HAP by VMD.<sup>56</sup> Thus, the effect of each orientation on the formation of the whole bFGF–FGFR–heparin complex is reproduced in Figure 6, which is involved in the biological functions mediated through the FGF/FGFR signaling pathway.<sup>4</sup> In the HP-up orientation, the adsorbed residues are located near the contact region of bFGF and FGFR, which may hamper the bFGF–FGFR interaction by a steric hindrance effect (Figure 6a). Also, the HP-down orientation is not beneficial to the formation of the bFGF–FGFR–heparin complex because of the adsorbed residues near the contact region of bFGF–FGFR–heparin (Figure 6c). However, in the HP-middle orientation, the bFGF–FGFR–heparin complex can be favorably formed because the adsorbed



**Figure 5.** Heparin-binding site and two DGR sequences in the (a) heparin-binding-up (HP-up), (b) heparin-binding-middle (HP-middle), and (c) heparin-binding-down (HP-down) orientations. The heparin-binding site is in red; Asp–Gly–Arg (DGR) is in yellow.



**Figure 6.** 2:2:2 bFGF–FGFR–heparin ternary complex with either of the two bFGF molecules adsorbed on HAP in the (a) heparin-binding-up (HP-up), (b) heparin-binding-middle (HP-middle), and (c) heparin-binding-down (HP-down) orientations. The adsorbed bFGF is in red. In the bFGF–FGFR–heparin complex, two bFGFs are cyan, two FGFRs are white, and two heparins are small red clusters.

**Table 2.** Major Adsorption Residues with Their Relative Residence Times, Energy Terms, Hydrogen Bonds, Distances to HAP, and Adsorption Sites in the HP-Up, HP-Middle, and HP-Down Orientations

state	residues	relative residence time (%)	electrostatic interactions (kJ·mol <sup>−1</sup> )	VDW interactions (kJ·mol <sup>−1</sup> )	hydrogen bonds	average distance (nm)	adsorption site
HP-up	Lys145	100	−344 ± 31	17 ± 16	2–3	0.16	Ca(1) vacancy
	Arg60	100	−271 ± 32	6 ± 15	2–3	0.16	Ca(1) vacancy
	Asp19	100	−216 ± 42	4 ± 11	0–1	0.24	−COO <sup>−</sup> near Ca(1), −NH <sub>3</sub> near PO <sub>4</sub> <sup>3−</sup>
	Gln54	79.8	9 ± 8	−4 ± 1	0	0.37	near PO <sub>4</sub> <sup>3−</sup> , Ca(2)
	Gln56	87.1	−10 ± 4	−11 ± 2	0	0.37	near PO <sub>4</sub> <sup>3−</sup>
	Glu59	97.6	13 ± 4	−15 ± 1	0	0.35	near Ca(2), OH <sup>−</sup> column
HP-middle	Arg39	100	−211 ± 25	0.9 ± 13	~2	0.16	Ca(1) vacancy
	Lys77	100	−331 ± 29	13 ± 15	~2	0.16	Ca(1) vacancy
	Lys86	100	−352 ± 33	19 ± 17	2–3	0.16	Ca(1) vacancy
	Asp37	100	−209 ± 23	2 ± 10	0	0.25	near Ca(1)
	Arg72	99.2	−21 ± 10	−11 ± 2	0	0.36	near PO <sub>4</sub> <sup>3−</sup>
	Arg81	59.8	10 ± 8	−6 ± 2	0	0.40	near PO <sub>4</sub> <sup>3−</sup> , Ca(2)
	Leu83	78.8	0.5 ± 1	−6 ± 2	0	0.38	near PO <sub>4</sub> <sup>3−</sup> , Ca(2)
HP-down	Lys26	100	−286 ± 38	−3 ± 14	1–2	0.17	Ca(1) vacancy
	Lys46	100	−331 ± 33	15 ± 16	1–3	0.16	Ca(1) vacancy
	Lys145	100	−355 ± 31	23 ± 17	2–3	0.16	Ca(1) vacancy
	Asn101	33.6	0.9 ± 4	−10 ± 2	0	0.41	near PO <sub>4</sub> <sup>3−</sup>
	Tyr103	87.5	8 ± 11	−6 ± 2	0	0.36	near PO <sub>4</sub> <sup>3−</sup> , Ca(2)

residues stay away from the bFGF–FGFR–heparin complex contact regions (Figure 6b). Also, after the formation of the 2:2:2 bFGF–FGFR–heparin ternary complex (2:2:2 is the molar ratio for the bFGF–FGFR–heparin ternary complex), the DGR sequences on the other bFGF (unadsorbed) are exposed to solution, suggesting the possibility of binding to an integrin (Figure 6b). The sequential formation of the 2:2:2 bFGF–FGFR–heparin ternary complex was proposed by Ornitz.<sup>8</sup> One possibility for the formation of the bFGF–FGFR–heparin ternary complex on HAP could be as follows:

FGFR initially interacts with an adsorbed bFGF in the HP-middle orientation and is stabilized by heparin, a second heparin then stabilizes the second binding of another bFGF–FGFR complex, and finally, a 2:2 bFGF–FGFR signaling complex coupled by two heparins activates the FGF/FGFR signaling pathway.

The convergent orientation distribution in the second-stage REMD (Figure 2c) suggests that when bFGF adsorbs on HAP surfaces nearly half of the population (in the HP-middle orientation) will support both the FGF–FGFR and DGR–



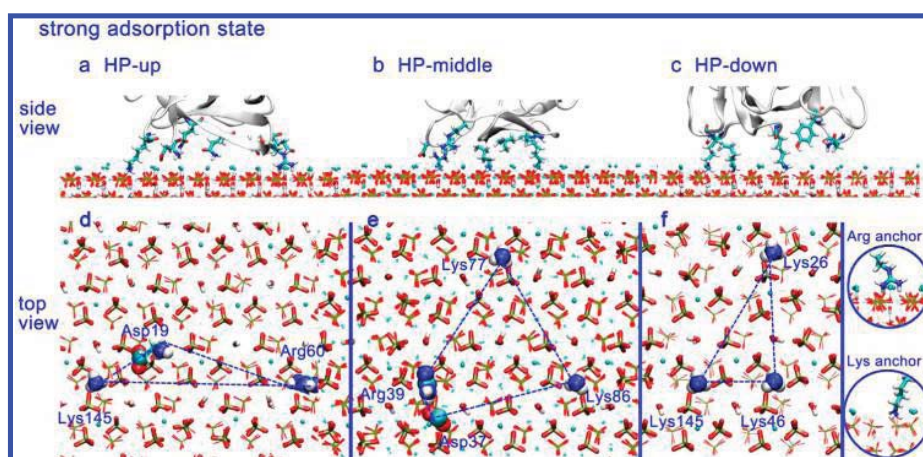


**Figure 7.** Adsorbed residues of bFGF (side view) and adsorption sites on the HAP surface (top view) in the (a, d) heparin-binding-up (HP-up), (b, e) heparin-binding-middle (HP-middle), and (c, f) heparin-binding-down (HP-down) orientations. The amino group of lysine and the guanidine group of arginine are presented in ball style. Enlarged side views for lysine and arginine anchoring are shown on the right.

integrin signaling pathways and the other half (in the HP-up and HP-down orientations) will support cell attachment through the DGR–integrin signaling pathway. The majority population ( $\sim 80\%$ ) has the protein dipole directed outward under the electrostatic effect of the weakly positively charged HAP surface.<sup>50</sup> The preferred orientation of a protein with a dipole can be regulated by surfaces with different charge properties<sup>27–31</sup> or an external electric field<sup>57</sup> because the dipole of a protein tends to remain parallel to the direction of the electric field.

**3.3. Anchoring Interactions and Topological Matching.** The adsorbed residues of bFGF and the adsorption sites on HAP were investigated in the HP-up, HP-middle, and HP-down configurations. In CMD simulations, residues with a minimum residue–HAP distance below 0.4 nm are labeled. For those residues, the residue–HAP distances for each frame were recorded. Relative residence time is defined as the percentage of the duration time for a residue–HAP distance below 0.4 nm in a simulation. Adsorbed residues with a relative residence time  $>30\%$  in each orientation are listed in Table 2 with their residue–HAP interaction terms (electrostatic and VDW interactions and hydrogen bonds), average minimum residue–HAP distances, and adsorption sites on the HAP surface. Figure 7a–c presents illustrations for these adsorbed residues, and Figure 7d–f shows the adsorption sites on the HAP surface.

In the HP-up orientation, Lys145, Arg60, and Asp19 adsorb as the major bound residues (relative residence time = 100%) by strong electrostatic interactions of  $-216$  to  $-344$   $\text{kJ}\cdot\text{mol}^{-1}$  per residue (Table 2 and Figure 7a,d). The basic residues, Lys145 and Arg60, form the anchoring interactions with the Ca(1) vacancies on the HAP surface by their amino and guanidine groups, respectively (Figure 7, right). The Ca(1) vacancy is a strongly negative triangular region surrounded by a triad of phosphate groups (see Figure S2 in the Supporting Information); it is highly complementary to the positively charged basic residues, forming strong electrostatic interactions (Table 2). In the anchoring interactions, 2 to 3 hydrogen bonds are formed between the amino/guanidine group and the surrounding triad of phosphate ions, with a residue–HAP distance of  $\sim 0.16$  nm. The adsorption of Asp19 (the N-terminus of bFGF) on HAP is  $50$ – $120$   $\text{kJ}\cdot\text{mol}^{-1}$  weaker than

that of the basic residues (Lys145 and Arg60). The  $-\text{COO}^-$  of Asp19 adsorbs near the positive Ca(1) region, whereas  $-\text{NH}_3^+$  adsorbs near the negative  $\text{PO}_4^{3-}$  region (Figure 7d). With lower binding affinity, Asp19 adsorbs  $\sim 0.24$  nm away from the HAP surface. Lys145, Arg60, and Asp19 form a triangle region on the HAP surface that exhibits geometric stability (Figure 7d). Other residues such as Gln54, Gln56, and Glu59 play a much weaker role in the adsorption, with weak VDW attraction of  $-4$  to  $-15$   $\text{kJ}\cdot\text{mol}^{-1}$ , and they stay  $0.35$ – $0.37$  nm away from the HAP surface. These residues do not adsorb on specific sites on the HAP surface. Instead, they move around within a region.

In the HP-middle orientation, three basic residues (Arg39, Lys77, and Lys86) and one acidic residue (Asp37) adsorb prominently on HAP by strong electrostatic interactions of  $-209$  to  $-352$   $\text{kJ}\cdot\text{mol}^{-1}$  per residue (Table 2 and Figure 7b,e). The basic residues, Arg39, Lys77, and Lys86, form the anchoring interactions with 2 to 3 hydrogen bonds and contribute  $-210$  to  $-333$   $\text{kJ}\cdot\text{mol}^{-1}$  to the binding affinity, with a residue–HAP distance of  $\sim 0.16$  nm per residue. Together they match with the three Ca(1) vacancies that comprise an equilateral triangle on the HAP surface (Figure 7e). The acidic residue, Asp37, adsorbs onto the positively charged Ca(1) area with an electrostatic interaction of  $\sim 209$   $\text{kJ}\cdot\text{mol}^{-1}$ . The minimum residue–HAP distance is around  $0.25$  nm, which is the second shortest distance. The four bound residues (Arg39, Lys77, Lys86, and Asp37) adsorb in the four points of a quadrilateral, which geometrically stabilizes the protein adsorption (Figure 7e). Other residues such as Arg72, Arg81, and Leu83 stay over  $0.35$  nm away from the HAP surface with weak VDW attraction of  $-6$  to  $-11$   $\text{kJ}\cdot\text{mol}^{-1}$  (Table 2).

In the HP-down orientation, three basic residues, Lys26, Lys46, and Lys145, comprise the dominant anchoring residues and contribute  $-286$  to  $-332$   $\text{kJ}\cdot\text{mol}^{-1}$  per residue to the binding affinity (Table 2 and Figure 7c,f). Together they match with the three Ca(1) vacancies that form a right triangle (Figure 7f).

In the energetically favorable adsorptions, the major bound residues interact with HAP through strong electrostatic interactions of  $-209$  to  $-355$   $\text{kJ}\cdot\text{mol}^{-1}$  per residue. There are usually 2 to 3 basic residues that form the anchoring interactions, with an energy contribution of  $210$ – $332$   $\text{kJ}\cdot\text{mol}^{-1}$  per residue to the adsorption, or they are accompanied



by an acidic residue with an adsorption energy of  $\sim 207$  kJ·mol<sup>-1</sup>. The major bound residues together form a triangle or a quadrilateral on the surface and stabilize the orientation and adsorption geometrically, which indicates some topologic matching between the protein and the defective HAP surface. When adsorbed in the Ca(1) vacancy, lysine exhibits stronger electrostatic interactions ( $-286$  to  $-352$  kJ·mol<sup>-1</sup>) with the HAP surface than those of arginine ( $-211$  to  $-271$  kJ·mol<sup>-1</sup>). This is because lysine presents better geometric matching with the surrounding triad of phosphate ions than does arginine (Figure 7e).

#### 4. CONCLUSIONS

In this work, an atomic-level investigation of bFGF adsorption on the HAP (001) surface was carried out by a combination of REMD and CMD methods. In CMD, the protein cannot readily cross the surface water layer, whereas in REMD, the protein can cross the adsorption barrier from the surface water layer and go through weak, medium, and then strong adsorption states, with protein–HAP interactions of  $-800$  to  $-1400$  kJ·mol<sup>-1</sup> and an average protein–HAP distance of around  $0.15$ – $0.17$  nm. Consequently, three energetically preferred orientations are achieved with  $\cos \theta$  at  $0.70 \pm 0.10$ ,  $0.20 \pm 0.20$ , and  $-0.68 \pm 0.10$ , which are labeled as heparin-binding-up (HP-up), heparin-binding-middle (HP-middle), and heparin-binding-down (HP-down), respectively.

Representative configurations for the HP-up, HP-middle, and HP-down orientations were investigated by second-stage REMD and CMD. Stronger adsorption energies occupy a larger population in the adsorption and tend to induce a larger conformational change. The HP-middle orientation with the strongest adsorption energy ( $-1149 \pm 40$  kJ·mol<sup>-1</sup>) has the largest adsorption population ( $52.1$ – $52.6\%$ ) and exhibits the biggest conformational change (RMSD of  $0.26 \pm 0.01$  nm). The HP-down and HP-up orientations with smaller adsorption energies of  $-1022 \pm 55$  and  $-894 \pm 70$  kJ·mol<sup>-1</sup>, respectively, have smaller populations of  $27.4$ – $27.7\%$  and  $19.7$ – $20.5\%$  and present smaller RMSD values of  $0.21 \pm 0.01$  and  $0.19 \pm 0.01$  nm, respectively. The convergent distribution indicates that nearly half of the population (in the HP-middle orientation) will support both the FGF–FGFR and DGR–integrin signaling pathways and the other half (in the HP-up and HP-down orientations) will support cell attachment through the DGR–integrin signaling pathway. The majority population ( $\sim 80\%$ ) has the protein dipole directed outward under the electrostatic effect of the weakly positively charged HAP surface.

In the energetically favorable adsorptions, there are usually 2 to 3 basic residues that form the anchoring interactions of  $210$ – $332$  kJ·mol<sup>-1</sup> per residue or that are appended by an acidic residue with an adsorption energy of  $\sim 207$  kJ·mol<sup>-1</sup>. The major bound residues together form a triangle or a quadrilateral on the surface and stabilize the orientation and adsorption geometrically, which indicates some topologic matching between the protein and the defective HAP surfaces with Ca vacancies. When adsorbed in the Ca(1) vacancy, lysine exhibits stronger electrostatic interactions ( $-286$  to  $-352$  kJ·mol<sup>-1</sup>) with the HAP surface than does arginine ( $-211$  to  $-271$  kJ·mol<sup>-1</sup>), and it has a better geometric match with the surrounding triad of phosphate ions.

#### ■ ASSOCIATED CONTENT

##### Supporting Information

Crystal geometry and HAP force field parametrization; first-stage REMD; and second-stage REMD. This material is available free of charge via the Internet at <http://pubs.acs.org>.

#### ■ AUTHOR INFORMATION

##### Corresponding Author

\*Tel: +86 20 87114069; E-mail: [jianzhou@scut.edu.cn](mailto:jianzhou@scut.edu.cn).

##### Notes

The authors declare no competing financial interest.

#### ■ ACKNOWLEDGMENTS

This work was supported by the National Key Basic Research Program of China (no. 2013CB733500), the National Natural Science Foundation of China (nos. 21376089 and 91334202), the Fundamental Research Funds for the Central Universities (SCUT-2013ZM0073), and the State Key Laboratory of Materials-Oriented Chemical Engineering (KL12-05). The computational resources for this project were provided by SCUTGrid at South China University of Technology and the National Supercomputing Center in Shenzhen.

#### ■ REFERENCES

- (1) Holmes, R. E. Bone Regeneration within a Coralline Hydroxyapatite Implant. *Plast. Reconstr. Surg.* **1979**, *63*, 626–633.
- (2) Drobeck, H. P.; Rothstein, S. S.; Gumaer, K. I.; Sherer, A. D.; Slichter, R. G. Histologic Observation of Soft Tissue Responses to Implanted, Multifaceted Particles and Discs of Hydroxylapatite. *J. Oral Maxillofac. Surg.* **1984**, *42*, 143–149.
- (3) El-Ghannam, A. Bone Reconstruction: From Bioceramics to Tissue Engineering. *Expert Rev. Med. Devices* **2005**, *2*, 87–101.
- (4) Yun, Y. R.; Won, J. E.; Jeon, E.; Lee, S.; Kang, W.; Jo, H.; Jang, J. H.; Shin, U. S.; Kim, H. W. Fibroblast Growth Factors: Biology, Function, and Application for Tissue Regeneration. *J. Tissue Eng.* **2010**, *2010*, 1–18.
- (5) Baird, A.; Schubert, D.; Ling, N.; Guillemin, R. Receptor- and Heparin-Binding Domains of Basic Fibroblast Growth Factor. *Proc. Natl. Acad. Sci. U.S.A.* **1988**, *85*, 2324–2328.
- (6) Moscatelli, D. High and Low Affinity Binding Sites for Basic Fibroblast Growth Factor on Cultured Cells: Absence of a Role for Low Affinity Binding in the Stimulation of Plasminogen Activator Production by Bovine Capillary Endothelial Cells. *J. Cell Physiol.* **1987**, *131*, 123–130.
- (7) Springer, B. A.; Pantoliano, M. W.; Barbera, F. A.; Gunyuzlu, P. L.; Thompson, L. D.; Herblin, W. F.; Rosenfeld, S. A.; Book, G. W. Identification and Concerted Function of Two Receptor Binding Surfaces on Basic Fibroblast Growth Factor Required for Mitogenesis. *J. Biol. Chem.* **1994**, *269*, 26879–26884.
- (8) Ornitz, D. M. FGFs, Heparan Sulfate and FGFRs: Complex Interactions Essential for Development. *BioEssays* **2000**, *22*, 108–112.
- (9) Rusnati, M.; Tanghe, E.; Dell'Era, P.; Gualandris, A.; Presta, M.  $\alpha_3\beta_1$  Integrin Mediates the Cell-Adhesive Capacity and Biological Activity of Basic Fibroblast Growth Factor (FGF-2) in Cultured Endothelial Cells. *Mol. Biol. Cell* **1997**, *8*, 2449–2461.
- (10) Reinhart, B.; Lee, L. E. J. Integrin-Like Substrate Adhesion in RTG-2 Cells, a Fibroblastic Cell Line Derived from Rainbow Trout. *Cell Tissue Res.* **2002**, *307*, 165–172.
- (11) Schnettler, R.; Alt, V.; Dingeldein, E.; Pfefferle, H. J.; Kilian, O.; Meyer, C.; Heiss, C.; Wenisch, S. Bone Ingrowth in bFGF-Coated Hydroxyapatite Ceramic Implants. *Biomaterials* **2003**, *24*, 4603–4608.
- (12) Jeong, I.; Yu, H. S.; Kim, M. K.; Jang, J. H.; Kim, H. W. FGF2-Adsorbed Macroporous Hydroxyapatite Bone Granules Stimulate in Vitro Osteoblastic Gene Expression and Differentiation. *J. Mater. Sci.: Mater. Med.* **2010**, *21*, 1335–1342.

- (13) Tsurushima, H.; Marushima, A.; Suzuki, K.; Oyane, A.; Sogo, Y.; Nakamura, K.; Matsumura, A.; Ito, A. Enhanced Bone Formation Using Hydroxyapatite Ceramic Coated with Fibroblast Growth Factor-2. *Acta Biomater.* **2010**, *6*, 2751–2759.
- (14) Alt, V.; Pfeifferle, H. J.; Kreuter, J.; Stahl, J. P.; Pavlidis, T.; Meyer, C.; Mockwitz, J.; Wenisch, S.; Schnettler, R. Effect of Glycerol-L-Lactide Coating Polymer on Bone Ingrowth of bFGF-Coated Hydroxyapatite Implants. *J. Controlled Release* **2004**, *99*, 103–111.
- (15) Maehara, H.; Sotome, S.; Yoshii, T.; Torigoe, I.; Kawasaki, Y.; Sugata, Y.; Yuasa, M.; Hirano, M.; Mochizuki, N.; Kikuchi, M. Repair of Large Osteochondral Defects in Rabbits Using Porous Hydroxyapatite/Collagen (Hap/Col) and Fibroblast Growth Factor-2 (FGF-2). *J. Orthop. Res.* **2010**, *28*, 677–686.
- (16) Feito, M.; Lozano, R.; Alcaide, M.; Ramírez-Santillán, C.; Arcos, D.; Vallet-Regí, M.; Portolés, M.-T. Immobilization and Bioactivity Evaluation of FGF-1 and FGF-2 on Powdered Silicon-Doped Hydroxyapatite and Their Scaffolds for Bone Tissue Engineering. *J. Mater. Sci.: Mater. Med.* **2011**, *22*, 405–416.
- (17) Kim, H.; Camata, R. P.; Lee, S.; Rohrer, G. S.; Rollett, A. D.; Vohra, Y. K. Crystallographic Texture in Pulsed Laser Deposited Hydroxyapatite Bioceramic Coatings. *Acta Mater.* **2007**, *55*, 131–139.
- (18) Lin, K.; Xia, L.; Gan, J.; Zhang, Z.; Chen, H.; Jiang, X.; Chang, J. Tailoring the Nanostructured Surfaces of Hydroxyapatite Bioceramics to Promote Protein Adsorption, Osteoblast Growth, and Osteogenic Differentiation. *ACS Appl. Mater. Interfaces* **2013**, *5*, 8008–8017.
- (19) Mkhonto, D.; de Leeuw, N. H. A Computer Modelling Study of the Effect of Water on the Surface Structure and Morphology of Fluorapatite: Introducing a  $\text{Ca}_{10}(\text{PO}_4)_6\text{F}_2$  Potential Model. *J. Mater. Chem.* **2002**, *12*, 2633–2642.
- (20) Lee, W.; Dove, M.; Salje, E. Surface Relaxations in Hydroxyapatite. *J. Phys.: Condens. Matter* **2000**, *12*, 9829–9841.
- (21) Zahn, D.; Hochrein, O. Computational Study of Interfaces between Hydroxyapatite and Water. *Phys. Chem. Chem. Phys.* **2003**, *5*, 4004–4007.
- (22) Filgueiras, M. R. T.; Mkhonto, D.; de Leeuw, N. H. Computer Simulations of the Adsorption of Citric Acid at Hydroxyapatite Surfaces. *J. Cryst. Growth* **2006**, *294*, 60–68.
- (23) Pan, H.; Tao, J.; Xu, X.; Tang, R. Adsorption Processes of Gly and Glu Amino Acids on Hydroxyapatite Surfaces at the Atomic Level. *Langmuir* **2007**, *23*, 8972–8981.
- (24) Wu, C. Y.; Chen, M. J.; Xing, C. Molecular Understanding of Conformational Dynamics of a Fibronectin Module on Rutile (110) Surface. *Langmuir* **2010**, *26*, 15972–15981.
- (25) Makrodimitris, K.; Masica, D. L.; Kim, E. T.; Gray, J. J. Structure Prediction of Protein-Solid Surface Interactions Reveals a Molecular Recognition Motif of Statherin for Hydroxyapatite. *J. Am. Chem. Soc.* **2007**, *129*, 13713–13722.
- (26) Yang, C.; Peng, C.; Liao, C.; Zhou, J. Computer Simulations of Fibronectin Adsorption on Graphene Modified Titanium Dioxide Surfaces. *Acta Chim. Sinica* **2014**, *72*, 401–406.
- (27) Zhou, J.; Chen, S.; Jiang, S. Orientation of Adsorbed Antibodies on Charged Surfaces by Computer Simulation Based on a United-Residue Model. *Langmuir* **2003**, *19*, 3472–3478.
- (28) Zhou, J.; Zheng, J.; Jiang, S. Y. Molecular Simulation Studies of the Orientation and Conformation of Cytochrome C Adsorbed on Self-Assembled Monolayers. *J. Phys. Chem. B* **2004**, *108*, 17418–17424.
- (29) Zhou, J.; Tsao, H. K.; Sheng, Y. J.; Jiang, S. Y. Monte Carlo Simulations of Antibody Adsorption and Orientation on Charged Surfaces. *J. Chem. Phys.* **2004**, *121*, 1050–1057.
- (30) Xie, Y.; Zhou, J.; Jiang, S. Y. Parallel Tempering Monte Carlo Simulations of Lysozyme Orientation on Charged Surfaces. *J. Chem. Phys.* **2010**, *132*, 065101.
- (31) Xie, Y.; Liu, M.; Zhou, J. Molecular Dynamics Simulations of Peptide Adsorption on Self-Assembled Monolayers. *Appl. Surf. Sci.* **2012**, *258*, 8153–8159.
- (32) Earl, D. J.; Deem, M. W. Parallel Tempering: Theory, Applications, and New Perspectives. *Phys. Chem. Chem. Phys.* **2005**, *7*, 3910–3916.
- (33) Liao, C. Y.; Zhou, J. Replica Exchange Molecular Dynamics Simulations on the Folding of Trpzip4 Beta-Hairpin. *Acta Chim. Sinica* **2013**, *71*, 593–601.
- (34) Lin, E.; Shell, M. S. Convergence and Heterogeneity in Peptide Folding with Replica Exchange Molecular Dynamics. *J. Chem. Theory Comput.* **2009**, *5*, 2062–2073.
- (35) Periole, X.; Mark, A. E. Convergence and Sampling Efficiency in Replica Exchange Simulations of Peptide Folding in Explicit Solvent. *J. Chem. Phys.* **2007**, *126*, 014903.
- (36) Wilson, R. M.; Elliott, J. C.; Dowker, S. E. P. Rietveld Refinement of the Crystallographic Structure of Human Dental Enamel Apatites. *Am. Mineral.* **1999**, *84*, 1406–1414.
- (37) Hauptmann, S.; Dufner, H.; Brickmann, J.; Kast, S. M.; Berry, R. S. Potential Energy Function for Apatites. *Phys. Chem. Chem. Phys.* **2003**, *5*, 635–639.
- (38) Bhowmik, R.; Katti, K. S.; Katti, D. Molecular Dynamics Simulation of Hydroxyapatite–Polyacrylic Acid Interfaces. *Polymer* **2007**, *48*, 664–674.
- (39) Ago, H.; Kitagawa, Y.; Fujishima, A.; Matsuura, Y.; Katsube, Y. Crystal Structure of Basic Fibroblast Growth Factor at 1.6 Å Resolution. *J. Biochem.* **1991**, *110*, 360–363.
- (40) van der Spoel, D.; Lindahl, E.; Hess, B.; van Buuren, A. R.; Apol, E.; Meulenhoff, P. J.; Tieleman, D. P.; Sijbers, A. L. T. M.; Feenstra, K. A.; van Drunen, R., et al. Gromacs User Manual, version 4.5. www.gromacs.org.
- (41) Kaminski, G. A.; Friesner, R. A.; Tirado-Rives, J.; Jorgensen, W. L. Evaluation and Reparametrization of the OPLS-AA Force Field for Proteins via Comparison with Accurate Quantum Chemical Calculations on Peptides. *J. Phys. Chem. B* **2001**, *105*, 6474–6487.
- (42) Berendsen, H. J. C.; Grigera, J. R.; Straatsma, T. P. The Missing Term in Effective Pair Potentials. *J. Phys. Chem.* **1987**, *91*, 6269–6271.
- (43) Hu, Z.; Jiang, J. Assessment of Biomolecular Force Fields for Molecular Dynamics Simulations in a Protein Crystal. *J. Comput. Chem.* **2010**, *31*, 371–380.
- (44) Yeh, I.-C.; Berkowitz, M. L. Ewald Summation for Systems with Slab Geometry. *J. Chem. Phys.* **1999**, *111*, 3155–3162.
- (45) Hess, B.; Bekker, H.; Berendsen, H. J. C.; Fraaije, J. G. E. M. LINCS: A Linear Constraint Solver for Molecular Simulations. *J. Comput. Chem.* **1997**, *18*, 1463–1472.
- (46) Nosé, S. A Unified Formulation of the Constant Temperature Molecular Dynamics Methods. *J. Chem. Phys.* **1984**, *81*, 511–519.
- (47) Hoover, W. G. Canonical Dynamics: Equilibrium Phase–Space Distributions. *Phys. Rev. A* **1985**, *31*, 1695–1697.
- (48) Patriksson, A.; van der Spoel, D. A Temperature Predictor for Parallel Tempering Simulations. *Phys. Chem. Chem. Phys.* **2008**, *10*, 2073–2077.
- (49) Liu, J.; Liao, C.; Zhou, J. Multiscale Simulations of Protein G B1 Adsorbed on Charged Self-Assembled Monolayers. *Langmuir* **2013**, *29*, 11366–11374.
- (50) Liao, C.; Xie, Y.; Zhou, J. Computer Simulations of Fibronectin Adsorption on Hydroxyapatite Surfaces. *RSC Adv.* **2014**, *4*, 15759–15769.
- (51) Utesch, T.; Daminelli, G.; Mrogiński, M. A. Molecular Dynamics Simulations of the Adsorption of Bone Morphogenetic Protein-2 on Surfaces with Medical Relevance. *Langmuir* **2011**, *27*, 13144–13153.
- (52) Yang, C.; Peng, C.; Zhao, D.; Liao, C.; Zhou, J.; Lu, X. Molecular Simulations of Myoglobin Adsorbed on Rutile (100) and (001) Surfaces. *Fluid Phase Equilib.* **2014**, *362*, 349–354.
- (53) Wei, T.; Carignano, M. A.; Szeleifer, I. Lysozyme Adsorption on Polyethylene Surfaces: Why Are Long Simulations Needed? *Langmuir* **2011**, *27*, 12074–12081.
- (54) Neamtu, M.; Cotrut, C. E.; Filioareanu, A.; Petreus, T.; Neamtu, A. Molecular Dynamics Simulation of Fibroblast Growth Factors Receptors Activation. In *International Conference on Advancements of Medicine and Health Care through Technology*; Vlad, S.; Ciupa, R.; Nicu, A., Eds.; Springer: Berlin, Germany, 2009; pp 311–314.
- (55) Schlessinger, J.; Plotnikov, A. N.; Ibrahim, O. A.; Eliseenkova, A. V.; Yeh, B. K.; Yayon, A.; Linhardt, R. J.; Mohammadi, M. Crystal

Structure of a Ternary FGF-FGFR-Heparin Complex Reveals a Dual Role for Heparin in FGFR Binding and Dimerization. *Mol. Cell* **2000**, *6*, 743–750.

(56) Humphrey, W.; Dalke, A.; Schulten, K. VMD – Visual Molecular Dynamics. *J. Mol. Graphics* **1996**, *14*, 33–38.

(57) Xie, Y.; Liao, C.; Zhou, J. Effects of External Electric Fields on Lysozyme Adsorption by Molecular Dynamics Simulations. *Biophys. Chem.* **2013**, *179*, 26–34.